Decomposition of luminescent hydroxyapatite scaffolds in simulated body fluid

Fabian Martinez-Pallares[a], Manuel Herrera[b,*], Olivia A. Graeve[a,c,*]

[a] Program in Materials Science and Engineering, University of California San Diego, La Jolla, CA 92093-0418, USA
[b] Centro de Nanociencias y Nanotecnología, Universidad Nacional Autónoma de México, Ensenada, Baja California 22800, México
[c] Department of Mechanical and Aerospace Engineering, University of California San Diego, La Jolla CA, 92093-0411, USA

* Corresponding authors [OAG: Email: ograeve@ucsd.edu, URL: http://graeve.ucsd.edu, orcid.org/0000-0003-3599-0502; MH: Email: zaldivar@ens.cnyn.unam.mx, orcid.org/0000-0002-7179-654X]

ABSTRACT: We present a luminescence study investigating the dissolution of rare-earth doped hydroxyapatite scaffolds in simulated body fluid (SBF), aiming to assess the luminescence stability of Tb-, Ce-, and Eu-doped scaffolds over time. Our findings reveal a consistent decrease in luminescence emission intensity across all samples over a four-week period in which the scaffolds were immersed in the SBF. In addition, energy dispersive spectroscopy confirms a decrease in rare-earth ion concentration in the scaffolds with respect to time, whereas fluorescence spectroscopy shows the presence of rare-earth ions in the SBF, indicating the partial dissolution of the scaffolds over time. The use of rare-earth ions as luminescence markers provides insights into the mechanisms of apatite formation in hydroxyapatites. Thus, these scaffolds may find wider use in regenerative medicine, particularly in targeted drug delivery systems, where their luminescent properties have the potential to non-invasively track drug release.

KEYWORDS: Hydroxyapatite, rare earth, luminescence, scaffold, simulated body fluid

1. INTRODUCTION

Hydroxyapatite [HAp, $Ca_5(PO_4)_3(OH)$ or $Ca(I)_4Ca(II)_6(PO_4)_6(OH)_2$ based on the composition of the unit cell][1] is one of the most frequently used biomaterials in orthopedic surgery due to its capability to promote bone formation.[2] It is also considered a versatile biomaterial because of its ability to accept dopant element substitutions into its cation (Ca^{2+}) and anion (PO_4^{3-} or OH^-) sites.[3,4] Cationic substitutions can be achieved on Ca(I) and Ca(II) sites by divalent and trivalent ions such as Al^{3+},[5] La^{3+},[6] Fe^{3+},[7] Ce^{3+},[8] or Eu^{2+}/Eu^{3+},[9,10] which requires a charge balance that can be accommodated by the loss of a proton from the OH^- or by the generation of calcium vacancies.[9,11] Rare-earth ions have a particular affinity as substitutional elements in HAp because of their similarity in ionic radii to the calcium ions (*e.g.*, Ca^{2+} = 106 pm, Ce^{3+} = 107 pm, Eu^{3+} = 101 pm, and Tb^{3+} = 0.98 pm).[12] Such substitutions result in changes in the lattice parameter and crystallinity of these materials, which may significantly affect their biological, chemical, and physical properties. Consequently, rare-earth doped HAp has potential applications for drug delivery,[13,14] electrical stimulation in tissue engineering technologies,[15] antimicrobials,[16] and cell labeling.[17]

When doped with rare-earth ions such as Eu^{3+}, Ce^{3+}, Tb^{3+}, and Yb^{3+}, HAp exhibits characteristic emission peaks that correspond to the 4*f* to 5*d* transitions of the dopants,[9,18] with an emission intensity dependent on the ion concentration of the dopant.[19] Thus, rare-earth doped HAp can be used as a sensor in tissues and cells.[20] Most of the rare-earth ions employed when doping HAp possess a valence state of +3.[21] However, in previous work we have reported the presence of Eu^{2+} and Yb^{2+} in calcium-deficient HAp.[9,10,18] The presence of both valence states (+2 and +3) may have an impact on the well-known bone resorption process during bone remodeling.[22] Bone remodeling is executed by osteoclasts that resorb bone and osteoblasts that fill the resorption cavities with a bone matrix that subsequently becomes mineralized through a process of bone mineralization. The stimulation of osteoblasts in the process of bone mineralization is related to the ability of hydroxyapatite to release phosphorus and calcium ions from their structure.[23] This can be modulated by changing crystallinity, crystalline phase, and the calcium to phosphorus ratio.[24] Bertazzo *et al.*[25] proposed a mechanism for *in vivo* bone mineralization in hydroxyapatite implants, which initiates with the solubilization of the hydroxyapatite surface and the precipitation of the ions present in the biological fluids, forming an apatite layer, which may have a general composition of $Ca_5(PO_4)_3(OH)$ (hydroxyapatite), $Ca_5(PO_4)_3F$ (fluorapatite), or $Ca_5(PO_4)_3Cl$ (chlorapatite).[1] This process is followed by the absorption of proteins and organic material, along with the adhesion of cells, their proliferation, and ultimately the formation of new bone. The performance of an implant depends on its ability to form an apatite layer on the surface.[25] Furthermore, the formation of the apatite layer is linked to the solubility of the hydroxyapatite implant, although the formation of an apatite layer is not exclusively limited to the presence of dissolved calcium or phosphorus ions from the implant, since both ions would be available if the implant was immersed in a biological fluid. In fact, previous reports have demonstrated apatite formation on surfaces of SiO_2 gel, gel-derived TiO_2, ZrO_2 gel, Nb_2O_5 gel, and Ta_2O_5 gel, among others, immersed in simulated body fluid (SBF).[26–31] SBF usually contains Na^+, K^+, Ca^{2+}, Mg^{2+}, Cl^-, $(HCO_3)^-$, $(HPO_4)^{2-}$, and $(SO_4)^{2-}$, which may result in the deposition of oxides, such as CaO and P_2O_5, that nucleate and grow the apatite layer,[32] even if the implant is not hydroxyapatite.

Given that the solubility of HAp plays a crucial role in the bone mineralization process, the ability to monitor it is essential. Xie *et al.*[20] demonstrated the feasibility of monitoring the dissolution of europium-doped hydroxyapatite in acetic acid by measuring the amount of europium dissolved in the acid, providing a valuable approach to studying and understanding HAp solubilization in a solution. Nonetheless, a study of rare-earth doped hydroxyapatite solubility in the presence of SBF has not been reported before. In this work, we present a luminescence study on the solubilization of Eu^{2+}/Eu^{3+}-, Ce^{3+}-, and Tb^{3+}-doped HAp scaffolds in the presence of SBF. We determine that the photoluminescence emission from the scaffolds decrease in a linear manner with respect to soaking time in the SBF. From scanning electron microscopy and energy dispersive spectroscopy we also show the formation of an apatite layer on the surfaces of the scaffolds. Thus, demonstrating the possibility of monitoring the gradual dissolution and re-precipitation of hydroxyapatite in SBF, and contributing to an understanding of the dissolution stability of hydroxyapatite in physiological fluids and the use of rare-earth ions as luminescence markers for biomaterials. This approach not only facilitates a deeper understanding of the material's behavior in biological environments but also opens avenues for non-invasive tracking of implant integration and bioactivity.

2. EXPERIMENTAL PROCEDURE

Eu^{2+}/Eu^{3+}-, Ce^{3+}-, and Tb^{3+}-doped hydroxyapatite powders (HAp:Eu, HAp:Ce, and HAp:Tb) were synthesized by solution combustion synthesis.[33–41] The reagents used were calcium nitrate tetrahydrate [$Ca(NO_3)_2 \bullet 4H_2O$, 99%], ammonium hydrogen phosphate [$(NH_4)_2HPO_4$, 98%], and carbohydrazide [$CO(NHNH_2)_2$, 97%], acquired from Alfa Aesar (Ward Hill, MA). Cerium nitrate hexahydrate [$Ce(NO_3)_3 \bullet 6H_2O$, 99.9%] and terbium nitrate hexahydrate [$Tb(NO_3)_3 \bullet 6H_2O$, 99.9%] from Sigma Aldrich (Burlington, MA), and europium nitrate hexahydrate [$Eu(NO_3)_3 \bullet 6H_2O$, 99.9%] from Alfa Aesar, were used as sources of the rare-earth dopants. The HAp:RE powders were prepared by dissolving 26.872 mmol of $Ca(NO_3)_2 \bullet 4H_2O$

and 1.414 mmol of rare-earth dopant into 28.28 mL of deionized water. Separately, 17.538 mmol of $(NH_4)_2HPO_4$ were dissolved in 25.45 mL of deionized water. Quantities of the precursors (in grams) were obtained by weighing in a Cole-Parmer Symmetry PA 120 Series analytical balance. The $(NH_4)_2HPO_4$ solution was then added dropwise to the calcium and rare-earth ion solution under continuous stirring, maintaining a molar ratio of Ca+RE to P of 1.67. Subsequently, 4.035 g of carbohydrazide were dissolved into the mixed solution and placed in a Pyrex crystallization dish, to be introduced into a furnace preheated at 773 K until ignition occurred, within approximately 15 minutes. The resulting HAp:RE powders were calcined at 873 K for 4 hours. The calcined powders were characterized by X-ray diffraction on a Bruker D2 Phaser using CuKα radiation and a step size of 0.01° over a 2θ range of 20 to 70 degrees. Particle size distributions were determined on a Microtrac Nanotrac ULTRA dynamic light scattering system, dispersing approximately 5 mg of powder in 20 mL of deionized water, stirring for 15 minutes and ultrasonicating for 15 minutes.

The slurry used to form the scaffolds were prepared by mixing 4 g of the HAp:RE powder with 1 mL of deionized water. The scaffolds were extruded using a syringe with an 18G needle and dried in an oven at 343 K for 1 hour. The SBF was prepared by dissolving sodium chloride [NaCl, 99.5%], sodium bicarbonate [$NaHCO_3$, 99.7%], potassium chloride [KCl, 99.0%], dipotassium hydrogen phosphate [$K_2HPO_4 \bullet 3H_2O$, 98%], magnesium chloride [$MgCl_2 \bullet 6H_2O$, 98%], calcium chloride [$CaCl_2$, 99.0%], sodium sulfate [Na_2SO_4, 99.0%], and tris-(hydroxymethyl) aminomethane [$(CH_2OH)_3CNH_2$, 99.8%], acquired from Sigma Aldrich, and hydrochloric acid [HCl, 1N] acquired from Fisher Scientific (Waltham, MA), in deionized water and buffered to pH 7.40 at 309 K with HCl. The solution was prepared based on the method outlined by Kokubo *et al.*[42] The evaluation of the solubility was prescribed by soaking the scaffolds in SBF for 4 weeks in a concentration of 1 mg of scaffold to 1 mL of SBF. After each week a volume of scaffold of approximate dimensions 5 × 5 × 5 mm^3 was taken from each sample and analyzed using photoluminescence.

Energy dispersive spectroscopy (EDS) was utilized to determine elemental composition using an X-Max Oxford Instruments system with a detector size of 20 mm^2. The morphologies of the powders and scaffolds were evaluated by scanning electron microscopy (SEM) using a JEOL JIB-4500 instrument at 10 kV. Photoluminescence measurements were performed in a Hitachi F-4500 fluorescence spectrophotometer over a wavelength range of 200 to 800 nm. To enhance the luminescence emission from the europium ions present in the SBF solution, 50 mL of SBF were mixed with 5 mL of Perkin Elmer Delfia® enhancement solution and analyzed in a Cary Eclipse fluorescence spectrophotometer using an excitation wavelength of 395 nm.

3. RESULTS AND DISCUSSION

The doped HAp powders display a flake-like morphology (Figure 1a) with an average particle size of ~120 nm from dynamic light scattering (Figure 1b). Powder X-ray diffraction (Figure 2) verifies the phase purity and crystal structure of the doped samples corresponding to PDF #09-0432. These patterns agree with the hexagonal HAp phase (space group $P6_3/m$). In addition, the patterns exhibit a small peak at ~31°, which corresponds to beta tri-calcium phosphate (β-TCP, PDF #06-0426), present as a minor secondary phase. The β-TCP phase is formed during the combustion synthesis process, since the reaction reaches higher temperatures (973 K) that are amenable to the formation of this phase. The patterns do not show the formation of rare-earth oxides due to the small concentration of the dopants (~1 at.%, Table 1). The emission spectra of the HAp:Eu, HAp:Ce, and HAp:Tb powders (Figure 3), show the characteristic emission peaks for Eu^{3+}, Ce^{3+} and Tb^{3+} ions, respectively. HAp:Ce, under excitation at 265 nm, shows a broad band at 360 nm, attributed to the transitions $^2D_{3/2} \rightarrow {}^2F_{5/2}$ and $^2D_{3/2} \rightarrow {}^2F_{7/2}$ (labeled A and B).[43–45] The emission spectrum for HAp:Tb, under excitation at 228 nm, exhibits four peaks centered at 493, 547, 591 and 626 nm (labeled C, D, E and F), and corresponding to the transitions $^5D_4 \rightarrow {}^7F_6$, $^5D_4 \rightarrow {}^7F_5$, $^5D_4 \rightarrow {}^7F_4$ and $^5D_4 \rightarrow {}^7F_3$, respectively.[46] The emission bands marked G, H, I, and J, for HAp:Eu correspond to the transitions $^5D_0 \rightarrow {}^7F_1$, $^5D_0 \rightarrow {}^7F_2$, $^5D_0 \rightarrow {}^7F_3$ and $^5D_0 \rightarrow {}^7F_4$ with centers at 594, 617, 655 and 698 nm.[47]

Table 1 summarizes the EDS results of the scaffolds before and after immersion during the four weeks of testing in SBF. The Ca/P ratios for all samples are below the stoichiometric value of 1.67 for HAp, indicating that the materials correspond to Ca-deficient HAp. In addition, from Table 1, we observe a notable decrease in the concentration of rare-earth ions after immersion in SBF, attributed to the partial dissolution of the HAp:RE scaffolds. Specifically, europium experiences a substantial decline in concentration from 1.26 to 0.49 (~61% decrease), whereas cerium and terbium exhibit decreases of ~30% and ~40%, respectively. The provenance of the oxygen, phosphorus, and calcium signals originate from both the HAp scaffolds and the ions in SBF, and it is not possible to separate the contributions, but EDS can provide us information on sodium and chlorine, which are present in the scaffolds only after soaking and must be from the SBF, since HAp does not contain either ion in its structure. The concentrations correspond to 11.43%, 14.39%, and 13.04%, for the HAp:Eu, HAp:Ce, and HAp:Tb scaffolds, respectively. Also, the Ca/P ratio increases in all scaffolds, from 1.41 to 1.56 in HAp:Eu, 1.38 to 1.46 in HAp:Ce, and 1.30 to 1.46 in HAp:Tb. The change in the Ca/P ratio is a result of the formation of apatite on the surface of the scaffold, a process previously reported in apatite materials in the presence of SBF.[48–50] Figure 4 illustrates a representative surface of our scaffolds before (Figure 4a) and after (Figure 4b-c) immersion in SBF, visually supporting the apatite layer formation. According to the EDS analysis performed on the surface (Figure 4d), calcium, phosphorus and oxygen from the hydroxyapatite and/or the SBF are present. Sodium and chlorine are also found and must be originating from the SBF.

Figure 5 depicts the values of the areas under the curves of the photoluminescence emission spectra corresponding to the three scaffolds. All scaffolds exhibit a linear attenuation of the photoluminescence emission. However, HAp:Eu and HAp:Ce have more pronounced slopes of -188 and -254, respectively, whereas HAp:Tb is much more stable over time and exhibits a slope of -35 (see linear fits to data in Figure 5). As mentioned earlier, the concentrations of dopants from EDS (Table 1) decrease by 30%, 61%, and 40%, for cerium, europium, and terbium, respectively. Thus, there is no direct correlation between the luminescence signal strength and the decrease in ion concentration. From this, we conjecture that terbium has a weaker dependence of dopant concentration to photoluminescence emission, resulting in a more constant luminescence signal over the four-week timeframe of testing. It is also possible that the EDS results are not reliable for determination of ion concentration in our scaffolds due to significant surface rugosity.[51]

We tested the release of europium from the HAp:Eu scaffold into the SBF (Figure 6), and show that all peaks in the fluorescence spectrum of the SBF correspond to the characteristic emission of Eu^{3+}. The peaks centered at 488 nm, 539 nm, and 618 nm, correspond to the transitions $^5D_2 \rightarrow {}^7F_0$, $^5D_1 \rightarrow {}^7F_0$, and $^5D_0 \rightarrow {}^7F_2$, respectively. Thus, the weakening of the photoluminescence emission is due to the partial dissolution of the scaffolds into the SBF. Note that Figure 6 shows no signal for the SBF (dashed line) before immersion of the scaffold.

The mineralization mechanism of HAp has been discussed previously by Kim *et al.*[52] and Bertazzo *et al.*[25] According to Kim *et al.*[52] the negative charge on the surface of HAp enables the attraction of positively charged calcium ions from the SBF. This attraction results in the formation of a calcium-rich amorphous apatite. Subsequently, these positive charges selectively bind with negatively charged phosphate ions present in the SBF, leading to the formation of a calcium-poor apatite structure. In contrast, Bertazzo *et al.*[25] suggests that the first step involves the solubilization of HAp, followed by the precipitation of phosphate ions, leading to the formation of a "biological apatite" (apatite deficient in calcium). However, this model was originally proposed based on reactions reported by Dorozhkin[53,54] for the HAp dissolution in different solutions that did not specifically examine the behavior in SBF.

In this study, we have determined that the combined analyses of europium fluorescence found in SBF (Figure 6) and the photoluminescence attenuation described in Figure 5 are evidence of the partial dissolution of the HAp scaffold, from which we describe the dissolution and reprecipitation process as follows. As a first step (Figure 7a), Ca^{2+}, PO_4^{3-}, and the rare-earth ions are dissolved in the SBF. The process of re-precipitation follows (Figure 7b), confirmed from images represented by Figure 4a-c, where a coating that is not present on the surface of the scaffold before immersion are now evident, and from the EDS analysis of Figure 4d, in which calcium and phosphorus from the SBF are seen, indicating the formation of apatite.[31,51,55] While our results do not show a homogeneous layer formed on the surface of the scaffolds, previous studies[25,52] suggest that the process of precipitation continues until equilibrium is achieved, resulting in a continuous apatite layer (Figure 7c).

Understanding the initial steps in the formation of apatite on doped HAp and determining its luminescence stability are crucial pieces of information for developing highly effective bioactive materials for medical applications. By knowing how apatite develops initially and the relevant timeframes for this, we can tailor biomaterials to encourage this process, ultimately enhancing their ability to integrate with biological tissues. Additionally, the stable luminescence of HAp, particularly HAp:Tb, ensures that these materials maintain their performance over time, a vital characteristic for their sustained effectiveness in medical applications. The application of rare-earth doped hydroxyapatite scaffolds extends beyond scaffold dissolution monitoring. These materials hold promise for broader applications in regenerative medicine, including their use in platforms for targeted drug delivery systems where their luminescent properties could offer real-time insights into drug release dynamics and tissue response. Such capabilities underscore the need for interdisciplinary research efforts to fully explore and harness the potential of these innovative materials.

4. CONCLUSIONS

Rare-earth doped hydroxyapatite (HAp) was synthesized by solution combustion synthesis, with europium, cerium, and terbium as dopants. The powders display a flake-like morphology and a particle size distribution of around 120 nm. According to X-ray diffraction analysis, the dopant concentration does not modify the crystal structure of the hydroxyapatite. Due to the high temperatures reached during combustion, a phase of β-TCP was formed as a minor secondary phase. The presence of the rare-earth ions in the powders was confirmed by EDS measurements, revealing a concentration of 1.26%, 1.35%, and 1.33% for HAp:Eu, HAp:Ce, and HAp:Tb, respectively. Photoluminescence spectra show the corresponding emissions of Eu^{3+} (594, 617, 655 and 698 nm), Ce^{3+} (360 nm), and Tb^{3+} (493, 547, 591 and 626 nm). After synthesis, the powders were used to prepare scaffolds using a solid free-form fabrication technique, then were soaked in simulated body fluid for four weeks, where it was found that the scaffolds were partially dissolved by SBF, and exhibited a linear attenuation of the emission. Fluorescence analysis of the SBF revealed the presence of dissolved europium in the fluid. The mineralization on the surface of the scaffolds can be explained by a simple solubilization, precipitation, and subsequent formation of an apatite layer.

Acknowledgements

This work was supported by a grant from the National Science Foundation (#1911372) and the UC-MEXUS program (No. CN19-137). The electron microscopy was performed at the San Diego Nanotechnology Infrastructure of UC San Diego, a member of the National Nanotechnology Coordinated Infrastructure, which is supported by the National Science Foundation.

Competing Interests

The authors declare no competing financial interests.

REFERENCES

(1) White, T.; Ferraris, C.; Kim, J.; Madhavi, S. Apatite - an adaptive framework structure. *Rev. Mineral. Geochem*. **2005**, *57* (1), 307–401. DOI: 10.2138/rmg.2005.57.10

(2) Šupová, M. Substituted hydroxyapatites for biomedical applications: A review. *Ceram. Int.* **2015**, *41* (8), 9203–923. DOI: 10.1016/j.ceramint.2015.03.316

(3) Ressler, A.; Žužić, A.; Ivanišević, I.; Kamboj, N.; Ivanković, H. Ionic substituted hydroxyapatite for bone regeneration applications: A review. *Open Ceram.* **2021**, *6*, 100122. DOI: 10.1016/j.oceram.2021.100122

(4) Tite, T.; Popa, A.- C.; Balescu, L. M.; Bogdan, I. M.; Pasuk, I.; Ferreira, J. M. F.; Stan, G. E. Cationic substitutions in hydroxyapatite: Current status of the derived biofunctional effects and their in vitro interrogation methods. *Materials (Basel)* **2018**, *11* (11), 2081. DOI: 10.3390/ma11112081

(5) Kolekar, T. V.; Thorat, N. D.; Yadav, H. M.; Magalad, V. T.; Shinde, M. A.; Bandgar, S. S.; Kim, J. H.; Agawane, G. L. Nanocrystalline hydroxyapatite doped with aluminium: A potential carrier for biomedical applications. *Ceram. Int.* **2016**, *2* (4), 5304–5311. DOI: 10.1016/j.ceramint.2015.12.060

(6) Webster, T. J.; Massa-Schlueter, E. A.; Smith, J. L.; Slamovich, E. B. Osteoblast response to hydroxyapatite doped with divalent and trivalent cations. *Biomaterials.* **2004**, *25* (11), 2111–2121. DOI: 10.1016/j.biomaterials.2003.09.001

(7) Jose, S.; Senthilkumar, M.; Elayaraja, K.; Haris, M.; George, A.; Dhayal Raj, A.; Sundaram, S. J.; Bashir, A. K. H.; Maaza, M.; Kaviyarasu, K. Preparation and characterization of Fe doped *n*-hydroxyapatite for biomedical application. *Surf. Interfaces.* **2021**, *25*, 101185. DOI: 10.1016/j.surfin.2021.101185

(8) Feng, Z.; Liao, Y.; Ye, M. Synthesis and structure of cerium-substituted hydroxyapatite. *J. Mater. Sci. - Mater. Med.* **2005**, *16*, 417–421. DOI: 10.1007/s10856-005-6981-8

(9) Zavala-Sanchez, L. A.; Hirata, G. A.; Novitskaya, E.; Karandikar, K.; Herrera, M.; Graeve, O. A. Distribution of Eu^{2+} and Eu^{3+} ions in hydroxyapatite: A

cathodoluminescence and Raman study, *ACS Biomater. Sci. Eng.* **2015**, *1* (12), 1306–1313. DOI: 10.1021/acsbiomaterials.5b00378

(10) Graeve, O. A.; Kanakala, R.; Madadi, A.; Williams, B. C.; Glass, K. C. Luminescence variations in hydroxyapatites doped with Eu^{2+} and Eu^{3+} ions. *Biomaterials*. **2010**, *31* (15), 4259–4267. DOI: 10.1016/j.biomaterials.2010.02.009

(11) Serret, A.; Cabañas, M. V.; Vallet-Regi, M. Stabilization of calcium oxyapatites with lanthanum(III)-created anionic vacancies. *Chem. Mater*. **2000**, *12* (12), 3836–3841. DOI: 10.1021/cm001117p

(12) Shannon, R. D. Revised effective ionic radii and systematic studies of interatomic distances in halides and chalcogenides. *Acta Crystallogr., Sect. A: Found. Crystallogr.* **1976**, *32* (5), 751–762. DOI: 10.1107/S0567739476001551

(13) Yang, P.; Quan, Z.; Li, C.; Kang, X.; Lian, H.; Lin, J. Bioactive, luminescent and mesoporous europium-doped hydroxyapatite as a drug carrier. *Biomaterials*. **2008**, *29* (32), 4341–4347. DOI: 10.1016/j.biomaterials.2008.07.042

(14) Ahymah Joshy, M. I.; Elayaraja, K.; Suganthi, R. V.; Chandra Veerla, S.; Kalkura, S. N. *In vitro* sustained release of amoxicillin from lanthanum hydroxyapatite nano rods. *Curr. Appl. Phys*. **2011**, *11* (4), 1100–1106. DOI: 10.1016/j.cap.2011.02.003

(15) Li, Y.; Ooi, C. P.; Cheang, P. H. N.; Khor, K. A. Synthesis and characterization of neodymium(III) and gadolinium(III)-substituted hydroxyapatite as biomaterials. *Int. J. Appl. Ceram. Technol*. **2009**, *6* (4), 501–512. DOI: 10.1111/j.1744-7402.2008.02293.x

(16) Lin, Y.; Yang, Z.; Cheng, J. Preparation, characterization and antibacterial property of cerium substituted hydroxyapatite nanoparticles. *J. Rare Earths* **2007**, *25* (4), 452–456. DOI: 10.1016/S1002-0721(07)60455-4

(17) Zantye, P.; Fernandes, F.; Ramanan, S. R.; Kowshik, M. Rare earth doped hydroxyapatite nanoparticles for in vitro bioimaging applications. *Curr. Phys. Chem.* **2019**, *9* (2), 94–109. DOI: 10.2174/1877946809666190828104812

(18) Zavala, L. A.; Fernández, P.; Novitskaya, E.; Díaz, J. N.; Herrera, M.; Graeve, O. A. Interconfigurational and intraconfigurational transitions of Yb^{2+} and Yb^{3+} ions in hydroxyapatite: A cathodoluminescence study. *Acta Mater.* **2017**, *135*, 35–43. DOI: 10.1016/j.actamat.2017.06.003

(19) Popa, C. L.; Ciobanu, C. S. Synthesis and characterization of fluorescent hydroxyapatite. *Rom. Rep. Phys.* **2016**, *68* (3), 1170–1177.

(20) Xie, Y.; Perera, T. S. H.; Li, F.; Han, Y.; Yin, M. Quantitative detection method of hydroxyapatite nanoparticles based on Eu^{3+} fluorescent labeling in vitro and in vivo. *ACS Appl. Mater. Interfaces* **2015**, *7* (43), 23819–23823. DOI: 10.1021/acsami.5b08767

(21) Gu, M.; Li, W.; Jiang, L.; Li, X. Recent progress of rare earth doped hydroxyapatite nanoparticles: Luminescence properties, synthesis and biomedical applications. *Acta Biomater.* **2022**, *148*, 22–43. DOI: 10.1016/j.actbio.2022.06.006

(22) Wu, L.; Yang, F.; Xue, Y.; Gu, R.; Liu, H.; Xia, D.; Liu, Y. The biological functions of europium-containing biomaterials: A systematic review. *Mater. Today Bio* **2023**, *19*, 100595. DOI: 10.1016/j.mtbio.2023.100595

(23) Jeong, J.; Kim, J. H.; Shim, J. H.; Hwang, N. S.; Heo, C. Y. Bioactive calcium phosphate materials and applications in bone regeneration. *Biomater. Res.* **2019**, *23*, 4. DOI: 10.1186/s40824-018-0149-3

(24) Dorozhkin S. V. Calcium orthophosphate-based bioceramics. *Materials (Basel)* **2013**, *6* (9), 3840–3942. DOI: 10.3390/ma6093840

(25) Bertazzo, S.; Zambuzzi, W. F.; Campos, D. D. P.; Ogeda, T. L.; Ferreira, C. V.; Bertran, C. A. Hydroxyapatite surface solubility and effect on cell adhesion. *Colloids Surf., B* **2010**, *78* (2), 177–184. DOI: 10.1016/j.colsurfb.2010.02.027

(26) Li, P.; Ohtsuki, C.; Kokubo, T.; Nakanishi, K.; Soga, N.; Nakamura, T.; Yamamuro, T. Apatite formation induced by silica gel in a simulated body fluid. *J. Am. Ceram. Soc.* **1992**, *75* (8), 2094–2097. DOI: 10.1111/j.1151-2916.1992.tb04470.x

(27) Li, P.; Ohtsuki, C.; Kokubo, T.; Nakanishi, K.; Soga, N.; De Groot, K. The role of hydrated silica, titania, and alumina in inducing apatite on implants. *J. Biomed. Mater. Res.* **1994**, *28* (1), 7–15. DOI: 10.1002/jbm.820280103

(28) Uchida, M.; Kim, H. -M.; Kokubo, T.; Miyaji, F.; Nakamura, T. Bonelike apatite formation induced on zirconia gel in a simulated body fluid and its modified solutions. *J. Am. Ceram. Soc.* **2001**, *84* (9), 2041–2044. DOI: 10.1111/j.1151-2916.2001.tb00955.x

(29) Miyazaki, T.; Kim, H. -M.; Kokubo, T.; Ohtsuki, C.; Nakamura, T. Apatite-forming ability of niobium oxide gels in a simulated body fluid. *J. Ceram. Soc. Jpn.* **2001**, *109* (1275), 929–933. DOI: 10.1002/jbm.820280103

(30) Miyazaki, T.; Kim, H. -M.; Kokubo, T.; Kato, H.; Nakamura, T. Induction and acceleration of bonelike apatite formation on tantalum oxide gel in simulated body fluid. *J. Sol-Gel Sci. Technol.* **2001**, *21*, 83–88. DOI: 10.1023/A:1011265701447

(31) Yamaguchi, S.; Nath, S.; Sugawara, Y.; Divakarla, K.; Das, T.; Manos, J.; Chrzanowski, W.; Matsushita, T.; Kokubo, T. Two-in-one biointerfaces–Antimicrobial and bioactive nanoporous gallium titanate layers for titanium implants. *Nanomaterials (Basel)*, **2017**, *7* (8), 229. DOI: 10.3390/nano7080229

(32) Pan, H.; Zhao, X.; Darvell, B. W.; Lu, W. W. Apatite-formation ability – predictor of "bioactivity"?. *Acta Biomater*. **2010**, *6* (11), 4181–4188 (2010). DOI: 10.1016/j.actbio.2010.05.013

(33) Novitskaya, E.; Manheim, A.; Herrera, M.; Graeve, O. A. Effect of oxygen vacancies on the mechanoluminescence response of magnesium oxide. *J. Phys. Chem. C* **2021**, *125* (1) 854–864. DOI: 10.1021/acs.jpcc.0c07674

(34) Novitskaya, E., Kelly, J. P., Bhaduri, S., Graeve, O. A. A review of solution combustion synthesis: An analysis of parameters controlling powder characteristics. *Int. Mater. Rev*. **2021**, *66* (3), 188–214. DOI: 10.1080/09506608.2020.1765603

(35) Kanakala, R.; Escudero, R.; Rojas-George, G.; Ramisetty, M.; Graeve, O. A. Mechanisms of combustion synthesis and magnetic response of high-surface-area hexaboride compounds. *ACS Appl. Mater. Interfaces* **2011**, *3* (4), 1093–1100. DOI: 10.1021/am1012276

(36) Kanakala, R.; Rojas-George, G.; Graeve, O. A. Unique preparation of hexaboride nanocubes: A first example of boride formation by combustion synthesis. *J. Am. Ceram. Soc*. **2010**, *93* (10), 3136–3141. DOI: 10.1111/j.1551-2916.2010.03853.x

(37) Sinha, K.; Pearson, B.; Casolco, S. R.; Garay, J. E.; Graeve, O. A. Synthesis and consolidation of $BaAl_2Si_2O_8$:Eu. Development of an integrated process for luminescent smart ceramic materials. *J. Am. Ceram. Soc*. **2009**, *92* (11), 2504–2511. DOI: 10.1111/j.1551-2916.2009.03242.x

(38) Graeve, O. A.; Varma, S.; Rojas-George, G.; Brown, D. R.; Lopez, E. A. Synthesis and characterization of luminescent yttrium oxide doped with Tm and Yb. *J. Am. Ceram. Soc*. **2006**, *89* (3), 926–931. DOI: 10.1111/j.1551-2916.2006.00845.x

(39) Lopez, O. A.; McKittrick, J.; Shea, L. E. Fluorescence properties of polycrystalline Tm^{3+}-activated $Y_3Al_5O_{12}$ and Tm^{3+}-Li^+ co-activated $Y_3Al_5O_{12}$ in the visible and near IR ranges. *J. Lumin.* **1997**, *71* (1), 1–11. DOI: 10.1016/S0022-2313(96)00123-8

(40) Shea, L. E.; McKittrick, J.; Lopez, O. A.; Sluzky, E.; Phillips, M. L. F. Advantages of self-propagating combustion reactions for synthesis of oxide phosphors. *J. Soc. Inf. Disp.* **1997**, *5* (2), 117–125. DOI: 10.1889/1.1985140

(41) Shea, L. E.; McKittrick, J.; Lopez, O. A.; Sluzky, E. Synthesis of red-emitting, small particle size luminescent oxides using an optimized combustion process. *J. Am. Ceram. Soc*. **1996**, *79* (12), 3257–3265. DOI: 10.1111/j.1151-2916.1996.tb08103.x

(42) Kokubo, T. Bioactive glass ceramics: Properties and applications. *Biomaterials*. **1991**, *12* (2), 155–163. DOI: 10.1016/0142-9612(91)90194-F

(43) Maleka, P. M.; Reddy, L.; Nkosi, T. J.; Balakrishna, A.; Kroon, R. E.; Swart, H. C.; Ntwaeaborwa, O. M. Structural and morphological characterization of photoluminescent cerium-doped near UV-blue sodium ortho-phosphate phosphors. *J. Lumin.* **2020**, *226*, 117409. DOI: 10.1016/j.jlumin.2020.117409

(44) Ghamami, S.; Anari, S. K.; Bakhshi, M.; Lashgari, A.; Salgado-Morán, G.; Glossman-Mitnik, D. Preparation and characterization of cerium (III) doped captopril nanoparticles and study of their photoluminescence properties. *Open Chem.* **2016**, *14* (1), 60–64. DOI: 10.1515/chem-2016-0008

(45) Kobylinska, N. G.; Dudarko, O. A.; Melnyk, I. V.; Seisenbaeva, G. A.; Kessler, V. G. Luminescence performance of cerium(III) ions incorporated into organofunctional mesoporous silica. *Microporous Mesoporous Mater*. **2020**, *305*, 110331. DOI: 10.1016/j.micromeso.2020.110331

(46) Nie, K.; Zhou, R.; Cheng, C. -A.; Duan, X.; Hu, Z.; Mei, L.; Liu, H.; Zhang, Y.; Wang, L.; Wang, H.; Ma, X. Structure, luminescence properties and energy transfer of terbium and samarium co-doped barium based apatite phosphor with tunable emission colour. *Heliyon* **2022**, *8* (12), e12566. DOI: 10.1016/j.heliyon.2022.e12566

(47) Verma, N.; Michalska-Domańska, M.; Ram, T.; Kaur, J.; Misra, A. K.; Dubey, V.; Dubey, N.; Tiwari, K.; Rao, M. C. Optimizing the luminescence efficiency of an europium (Eu^{3+}) doped SrY_2O_4 phosphor for flexible display and lighting applications. *RSC Adv*. **2023**, *13* (29), 20217–20228. DOI: 10.1039/d3ra03199c

(48) Demirtaş, T. T.; Kaynak, G.; Gümüşderelioğlu, M. Bone-like hydroxyapatite precipitated from 10×SBF-like solution by microwave irradiation. *Mater. Sci. Eng., C* **2015**, *49*, 713–719. DOI: 10.1016/j.msec.2015.01.057

(49) Spanos, N.; Misirlis, D. Y.; Kanellopoulou, D. G.; Koutsoukos, P. G. Seeded growth of hydroxyapatite in simulated body fluid. *J. Mater. Sci.* **2006**, *41*, 1805–1812. DOI: 10.1007/s10853-006-2952-9

(50) Cho, S. -B.; Nakanishi, K.; Kokubo, T.; Soga, N.; Ohtsuki, C.; Nakamura, T.; Kitsugo, T.; Yamamuro, T. Dependence of apatite formation on silica gel on its structure: Effect of heat treatment. *J. Am. Ceram. Soc*. **1995**, *78* (7), 1769–1774. DOI: 10.1111/j.1151-2916.1995.tb08887.x

(51) Goldstein, J. I.; Newbury, D. E.; Michael, J. R.; Ritchie, N. W. M.; Scott, J. H. J.; Joy, D. C. *Scanning Electron Microscopy and X-ray Microanalysis*, 4th ed.; Springer, 2018. DOI: 10.1007/978-1-4939-6676-9

(52) Kim, H. -M.; Himeno, T.; Kokubo, T.; Nakamura, T. Process and kinetics of bonelike apatite formation on sintered hydroxyapatite in a simulated body fluid. *Biomaterials* **2005**, *26* (21), 4366–4373. DOI: 10.1016/j.biomaterials.2004.11.022

(53) Dorozhkin, S. V. Surface reactions of apatite dissolution. *J. Colloid Interface Sci.* **1997**, *191* (2), 489–497. DOI: 10.1006/jcis.1997.4942

(54) Dorozhkin, S. V. Inorganic chemistry of the dissolution phenomenon: The dissolution mechanism of calcium apatites at the atomic (ionic) level. *Comments Inorg. Chem.* **1999**, *20* (4-6), 285–299. DOI: 10.1080/02603599908021447

(55) Zvicer, J.; Medic, A.; Veljovic, D.; Jevtic, S.; Novak, S.; Obradovic, B. Biomimetic characterization reveals enhancement of hydroxyapatite formation by fluid flow in gellan gum and bioactive glass composite scaffolds. *Polym. Test.* **2019**, *76*, 464–472. DOI: 10.1016/j.polymertesting.2019.04.004

Figures

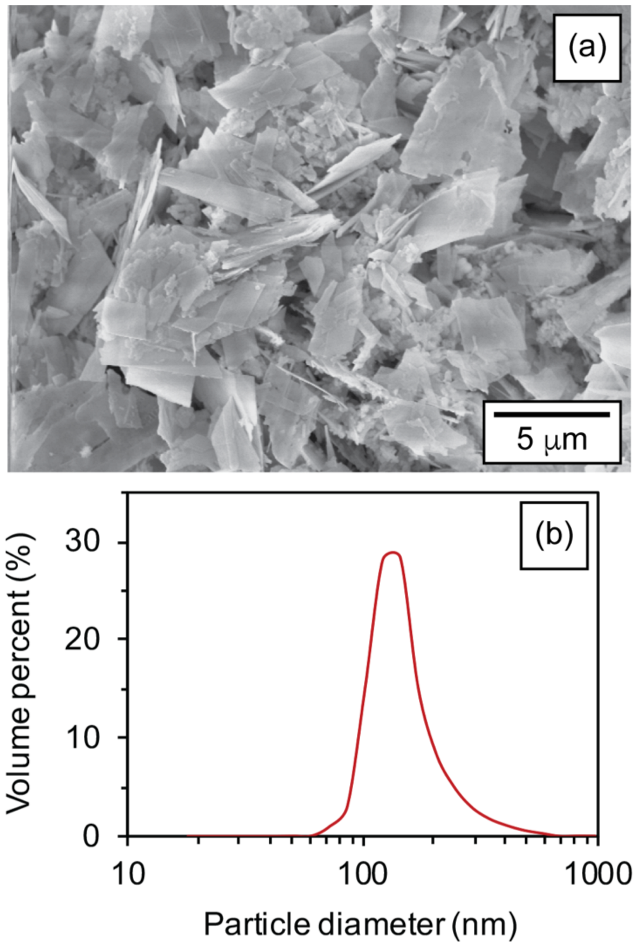

Figure 1. (a) Scanning electron micrograph and (b) particle size distribution of the combustion synthesized HAp powders.

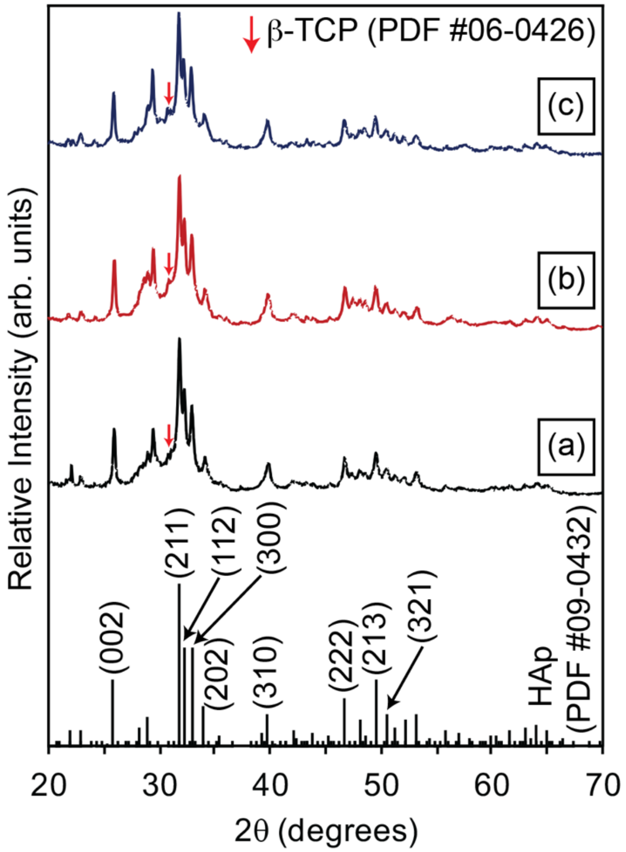

Figure 2. X-ray diffraction patterns of the (a) HAp:Eu, (b) HAp:Ce, and (c) HAp:Tb powders. The red arrow marks the location of the primary peak for β-TCP.

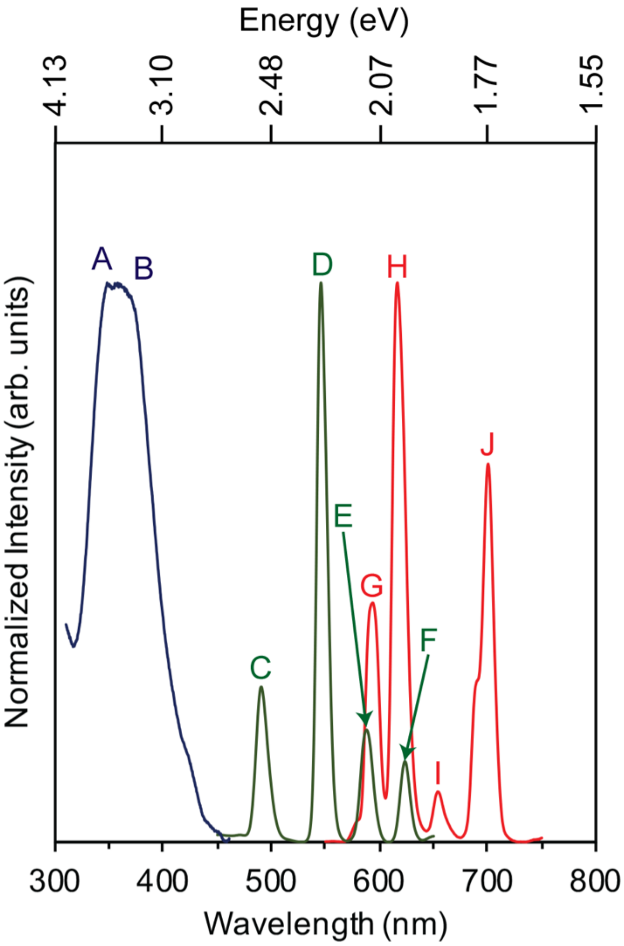

Figure 3. Photoluminescence emission spectra of HAp:Eu (red), HAp:Tb (green), and HAp:Ce (blue). A-B are the characteristic emission peaks for Ce^{3+}, C-F are the characteristic emission peaks for Tb^{3+}, and G-J are the characteristic emission peaks for Eu^{3+}.

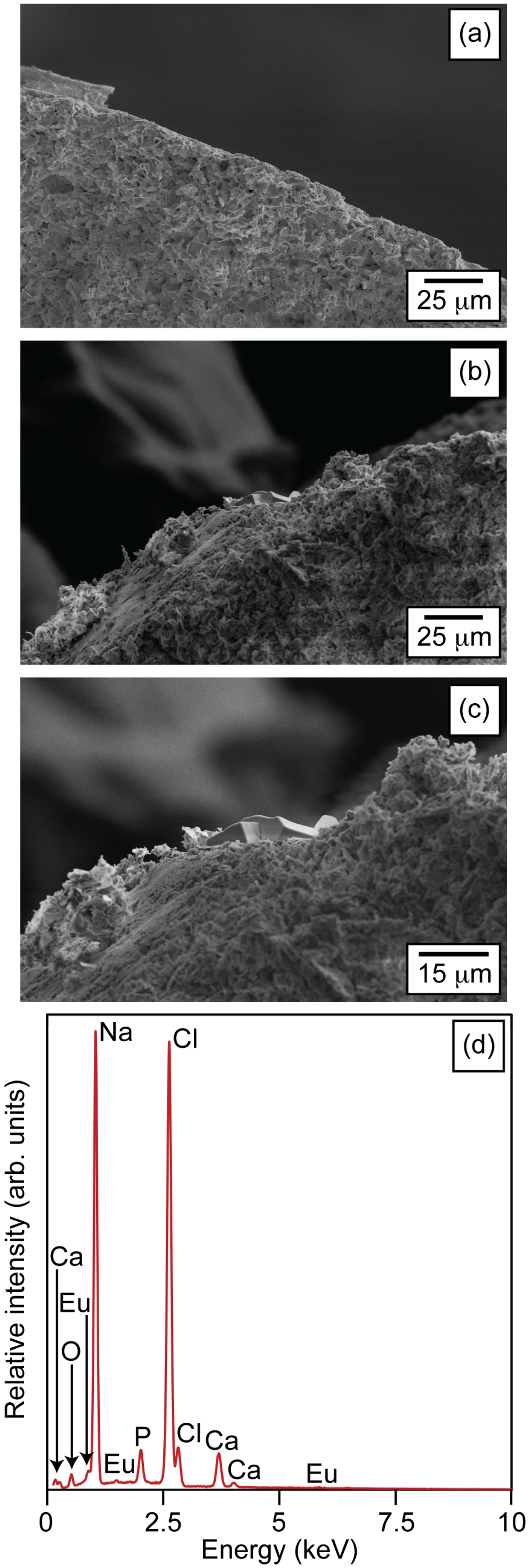

Figure 4. Scanning electron micrographs of a representative scaffold before (a), and after (b-c) immersion in simulated body fluid. (d) Energy dispersive spectrum of the scaffold surface after immersion for 4 weeks.

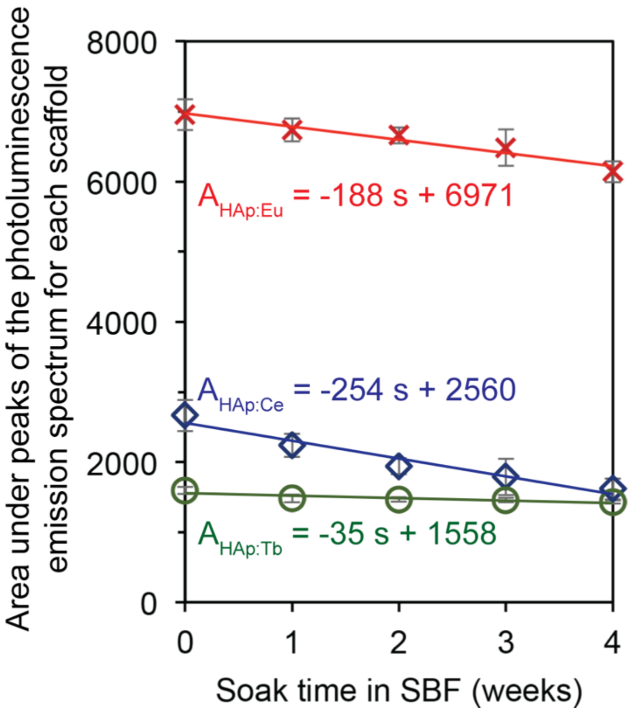

Figure 5. Area under peaks of the photoluminescence emission spectrum for the HAp:Eu, HAp:Ce, and HAp:Tb scaffolds.

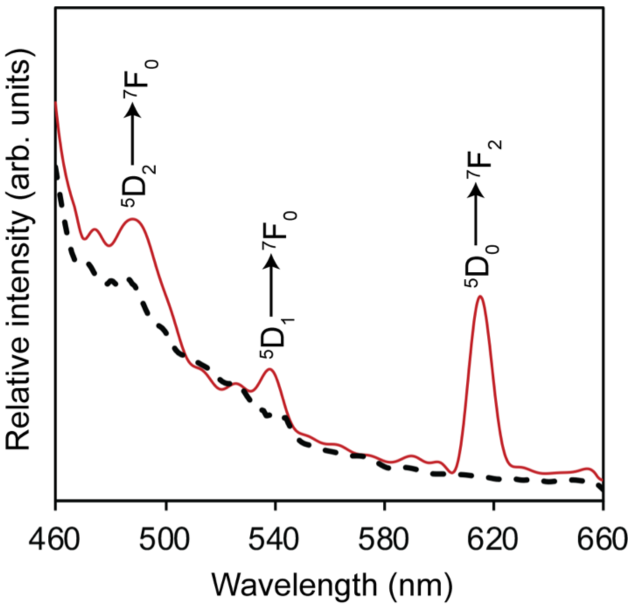

Figure 6. Fluorescence spectra of SBF before (dashed line) and after contact with the HAp:Eu scaffold for four weeks (solid line).

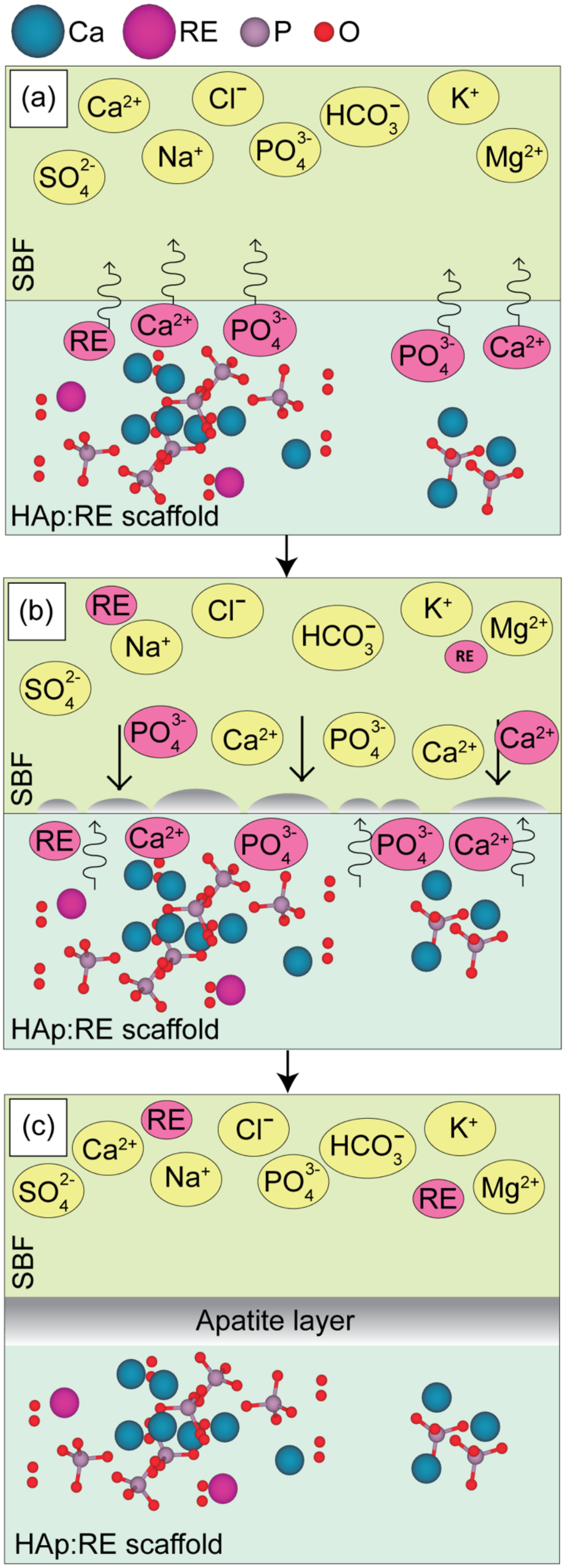

Figure 7. Schematic depicting surface changes in the HAp:RE scaffold during SBF immersion: (a) Initial HAp:RE surface solubilization, (b) ongoing HAp:RE surface solubilization concurrent with ion precipitation from SBF, primarily calcium and phosphorus, and (c) formation of an apatite layer upon reaching equilibrium between SBF and the HAp:RE surface.

Tables

Table 1. Elemental composition of the HAp:RE scaffolds before and after soaking in simulated body fluid for four weeks (determined from energy dispersive spectroscopy).

	O (at.%)	P (at.%)	Ca (at.%)	RE (at.%)	Na and Cl (at.%)	Ca/P
Before soaking in simulated body fluid						
HAp:Ce	57.32	17.38	23.95	1.35	-	1.38
HAp:Eu	55.98	17.73	25.03	1.26	-	1.41
HAp:Tb	57.57	17.85	23.25	1.33	-	1.30
After soaking in simulated body fluid						
HAp:Ce	46.55	15.51	22.59	0.95 (-30%)	14.39	1.46
HAp:Eu	50.51	14.66	22.91	0.49 (-61%)	11.43	1.56
HAp:Tb	47.86	15.37	22.94	0.81 (-40%)	13.04	1.49